



Original Paper

Pore-scale fluid distribution and remaining oil during tertiary low-salinity waterflooding in a carbonate



Chun-Yu Tong^{a, b}, Yong-Fei Yang^{a, b, *}, Qi Zhang^{a, b}, Gloire Imani^{a, b}, Lei Zhang^{a, b},
Hai Sun^{a, b}, Jun-Jie Zhong^{a, b}, Kai Zhang^{a, b}, Jun Yao^{a, b}

^a State Key Laboratory of Deep Oil and Gas, China University of Petroleum (East China), Qingdao, 266580, Shandong, PR China

^b School of Petroleum Engineering, China University of Petroleum (East China), Qingdao, 266580, Shandong, PR China

ARTICLE INFO

Article history:

Received 16 February 2024

Received in revised form

3 September 2024

Accepted 9 September 2024

Available online 10 September 2024

Edited by Yan-Hua Sun

Keywords:

Tertiary low-salinity waterflooding

Micro-CT

Wettability alteration

Digital core

Remaining oil

ABSTRACT

Low-salinity waterflooding, as a promising enhanced oil recovery method, has exhibited exciting results in various experiments conducted at different scales. For carbonate rock, pore-scale understanding of the fluid distribution and remaining oil after low-salinity waterflooding is essential, especially the geometry and topology analysis of oil clusters. We performed the tertiary low-salinity waterflooding and employed X-ray micro-CT to probe the pore-scale displacement mechanism, fluid configuration, oil recovery, and remaining oil distribution. We found that the core becomes less oil-wet after low-salinity waterflooding. Furthermore, we analyzed the oil-rock and oil-brine interfacial areas to further support the wettability alteration. By comparing images after high-salinity waterflooding and low-salinity waterflooding, it is proven that wettability alteration has a significant impact on the behavior of the two-phase flow. Our research demonstrates that low-salinity waterflooding is an effective tertiary enhanced oil recovery technology in carbonate, which changes the wettability of rock and results in less film and singlet oil. © 2024 The Authors. Publishing services by Elsevier B.V. on behalf of KeAi Communications Co. Ltd. This is an open access article under the CC BY-NC-ND license (<http://creativecommons.org/licenses/by-nc-nd/4.0/>).

1. Introduction

Carbonate reservoirs, as the most essential hydrocarbon source (Kargarpour, 2020), hold about 60% of the world's oil reserves (Akbar et al., 2000; Kargarpour, 2020). Nevertheless, the recovery factor in carbonate reservoirs is relatively low as a result of the significant heterogeneity (Xu et al., 2020). One of the methods suggested to improve oil recovery is low-salinity waterflooding (LSW), where the ionic composition and concentration of brines are changed or lowered (Bartels et al., 2017a; Smalley et al., 2018). Compared with the other existing methods, LSW has the advantage of being environment-friendly and cost-effective (Mokhtari et al., 2019; Tawfik et al., 2022). The method has received considerable attention since the log-inject-log field test showed a 20%–50% reduction in residual oil saturation (Webb et al., 2004). Several researchers have proposed that two categories of mechanisms were responsible for recovery improvement, namely, rock-fluid

interaction and fluid-fluid interaction (Lyu et al., 2022). It is imperative to note that the interactions between sandstone and carbonate reservoirs exhibit distinct characteristics. In carbonates, rock-fluid interaction includes multi-ion exchange (Haagh et al., 2017; Wei et al., 2017), electrical double layer (EDL) expansion (Nasralla and Nasr-El-Din, 2014; Koleini et al., 2019; Mehana et al., 2020; Farhadi et al., 2021), and mineral dissolution (Hiorth et al., 2010), while fluid-fluid interaction includes the formation of micro-dispersions (Mahzari and Sohrabi, 2014; Sohrabi et al., 2017), interfacial tension reduction (Tetteh et al., 2020), and fluid coalescence (Ayirala et al., 2018a, 2018b). The prevailing viewpoint in the literature indicates that the implementation of LSW induces a shift in wettability from an oil-wet state to a less oil-wet state (Bartels et al., 2017a; Berg et al., 2010). This wettability alteration has been seen to result in enhanced oil recovery, as evidenced by several experimental investigations conducted at the field scale (Webb et al., 2004) and core scale (Lager et al., 2008). More importantly, wettability governs the arrangement of the fluid within the pore (Blunt, 2017). Hence, modifying the wettability will result in a significant change in the fluid behavior. Therefore, it is necessary to clarify the fluid redistribution and remaining oil due to wettability alteration in carbonate reservoirs during LSW.

* Corresponding author. State Key Laboratory of Deep Oil and Gas, China University of Petroleum (East China), Qingdao 266580, Shandong, PR China.

E-mail address: yangyongfei@upc.edu.cn (Y.-F. Yang).

From the literature, it can be observed that studies about LSW are primarily concentrated on core and sub-pore scales (atomic scale and electronic scale). There is a gap between these scales in which more researches are needed (Bartels et al., 2016, 2017b). Micro-CT is an advanced tool that permits visualization of the fluid distribution during LSW. Lebedeva and Fogden (2011) investigated the oil recovery efficiency in quartz sand grains with or without kaolinite during LSW. Their results showed the highest recovery in clean sand (without kaolinite), while the lowest recovery in kaolinite-coated sand when performing high-salinity waterflooding (HSW). They also found that oil residuals from secondary LSW and tertiary LSW were comparable in quartz sand grains with kaolinite. Micro-CT was also utilized to study the low-salinity effect in Berea sandstones, revealing the occurrence of fines movement (Shabaninejad et al., 2018). By comparing secondary and tertiary LSW, Chen et al. (2021) investigated the role of initial brine distribution on remaining oil saturation, pointing out that initial brine distribution impeded recovery enhancement at the tertiary LSW while the secondary LSW displaced more oil by invading a wider variety of pores. Andrews et al. (2021) examined the phenomenon of wettability alteration and fluid redistribution. Their findings revealed that the effectiveness of LSW was associated with changes in wetting properties and pore structure. In another study, Andrews et al. (2023) conducted tertiary LSW in three sandstones to probe the relationship between pore structure and oil production. They found that there was a relationship between the connectivity in the largest pores and oil recovery, i.e., a higher oil recovery was obtained in Berea sandstone where the largest pores were poorly connected, while a lower oil recovery in the Castlegate sample where the largest pores were well connected. Furthermore, Mirchi (2018) investigated the synergistic interaction between LSW and surfactant using micro-CT. The study reported that in-situ contact angles decreased after a substantial pore volume injection of low-salinity brine. Additionally, it found that low-salinity surfactant injection of only one pore volume was adequate to shift local wettability from an oil-wet to a less oil-wet state. However, the works mentioned above are based on sandstones, whereas only a few X-ray imaging experiments were conducted in carbonate rocks (Bartels et al., 2016, 2017b; Qin et al., 2019; Selem et al., 2021, 2022, 2023). Particularly, the analysis of the geometry and topology of remaining oil after LSW in carbonate rocks is scarce.

Here, a carbonate rock was utilized to conduct a miniature core-flooding experiment. High- and low-salinity brine was injected under a capillary-dominated regime and micro-CT was used for image acquisition at the end of injection. Image segmentation was conducted to investigate pore-scale low-salinity effects that wettability alteration induces fluid redistribution. In addition, we classified the remaining oil clusters based on shape factor and Euler number. Saturation and statistical analysis of the remaining oil were also done. This study emphasizes that wettability alteration has effects on fluid configuration, especially, remaining oil distribution, guiding oil recovery from carbonate reservoirs.

2. Material and methods

2.1. Rock and fluid properties

The primary components of the rock sample were identified as calcite (95 wt%) using an X-ray diffraction instrument. A mini-core, with a diameter of 5 mm and a length of approximately 9 mm, was drilled from a standard core using air as a coolant. Based on the segmented image, we plotted its porosity profile (Fig. 1(a)). The segmented porosity was 8.97%, and the permeability assessed using the pore network model (Dong and Blunt, 2009) was 61.54 mD. Pore radius and throat radius distribution were also calculated

using the pore network model, as depicted in Fig. 1(b). Two distinct brines were used to conduct the flow experiment: high-salinity brine (HSB) was used to saturate rock samples and for secondary displacement, while low-salinity brine (LSB) was used for tertiary displacement. Table 1 presents the composition of high-salinity and low-salinity brines, and the fluid properties are listed in Table 2. All the brines used were prepared in the laboratory, where the ion composition and content of LSB were from Qin et al. (2019). The crude oil has a density of 0.792 g/cm³ at 20 °C, a viscosity of 2.741 mPa·s at 26 °C, and an asphaltene content of less than 1 wt%. It was doped with 16.7 vol% iododecane (98% purity, from Macklin) to enable contrast with brine and prevent changes in the brine's salinity. Note that iododecane does not contain any functional groups related to wettability alteration, so the impact of the dopant can be neglected (Chen et al., 2021).

2.2. Flow experiments

At first, the mini-core was placed into a carbon-fiber core holder. The dry mini-core was imaged as a reference image before the flow experiment. In this study, the CT equipment used to image mini-cores of various displacement stages was a MicroXCT-400 machine from Zeiss (Fig. 2). The distances separating the source and the sample, as well as the sample and the detector, were measured to be 43 and 22 mm, respectively, and the image resolution was 4.51 μm under a 4X lens. All the images before and after LSW were obtained at a voltage of 120 kV and a power of 10 W, and the exposure time was 5 s. The middle position of the core was selected during each scan to ensure that imaging was as in-situ as possible. Finally, reconstruction was conducted to create 3D tomograms that mapped the rock pore space and fluid distribution.

After acquiring the dry image, CO₂, which can dissolve in brine and oil, was injected into the mini-core to remove the air. Next, we began to conduct tertiary LSW following the steps below (Fig. 3). All the flow experiments (referred to as the displacement process) were performed at room temperature (20 °C) and atmospheric pressure (0.1 MPa), maintaining a confining pressure of approximately 7 MPa within the core holder to prevent fluid bypassing. HSB was injected into the core to achieve an original brine saturation equal to 1. Then, doped crude oil was injected into the mini-core, which became almost completely saturated with crude oil. The core holder was not taken out of the constant-temperature oven until 54 h at 60 °C to achieve aging. Note that the rock was originally oil-wet, aging was to ensure the integrity of the experiment rather than changing the wettability of the rock. Before waterflooding, fresh doped crude oil was reintroduced into the mini-core. Afterward, HSB of about 117 pore volumes (PVs) was pumped into the mini-core at a rate of 0.04 mL/min, and the core holder stood for about 13 h at 60 °C to make the system reach thermodynamic equilibrium. Lastly, LSB of nearly 158 pore volumes was injected at a rate of 0.04 mL/min, and the core holder was also held at 60 °C. Test scans were performed to achieve stable fluid distribution (steady state) after the flooding. Extremely high pore volumes of brine were injected to ensure that the recoverable oil was completely displaced. The interfacial tension between oil and HSB was 16.82 mN/m, and between oil and LSB was 18.20 mN/m. During the injection of HSB and LSB, the capillary numbers $N_c = v\mu/\sigma$ were 1.71×10^{-6} and 1.52×10^{-6} , respectively.

2.3. Image processing

After reconstruction, the images were imported into image analysis software (Avizo 2019). The data, comprising $988 \times 1013 \times 986$ voxels, was filtered using the non-local means filter to eliminate noise and ring artifacts, as illustrated in Fig. 4(a).

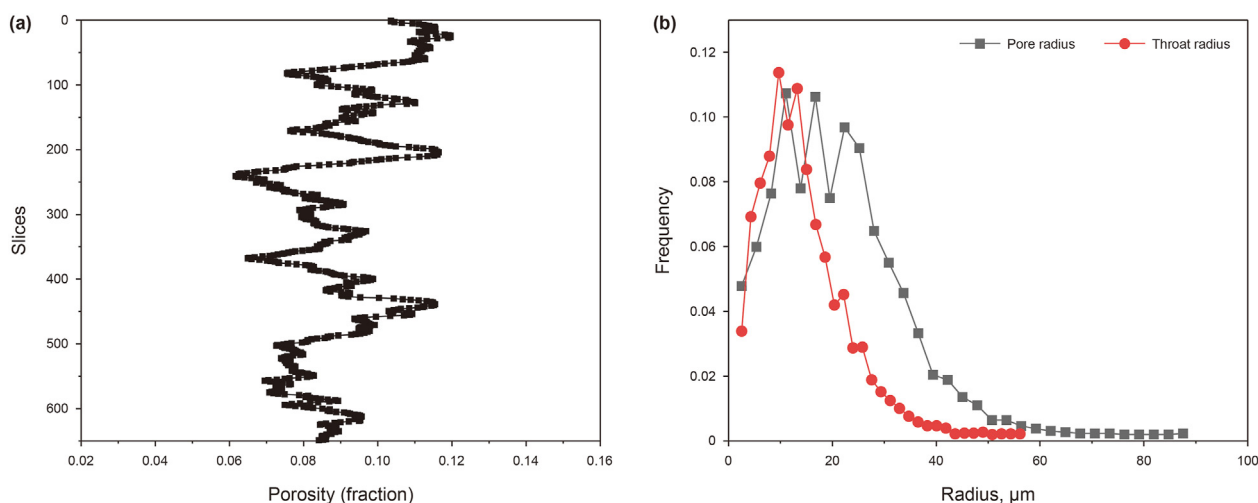


Fig. 1. (a) Porosity distribution from inlet to outlet of the sample; (b) Distribution of pore and throat radius.

Table 1
Composition of high-salinity brine and low-salinity brine.

Brine	Composition, g/L					Total dissolved salts, g/L
	NaCl	KCl	CaCl ₂	MgCl ₂	Na ₂ SO ₄	
High-salinity brine	115.77	1.49	26.41	4.0	–	147.67
Low-salinity brine	–	–	0.562	0.2	0.8	1.562

Table 2
Properties of high-salinity brine, low-salinity brine, and oil used.

Fluid	Density @ 20 °C, kg/m ³	Viscosity @ 26 °C, mPa·s
Oil	792.0	2.741
High-salinity brine	996.4	0.846
Low-salinity brine	983.0	0.846

The filtered images containing oil and brine were then registered using the dry image as a reference to make sure that both images were in pixel-by-pixel superposition. Afterward, we cropped images with dimensions of 650 μm × 650 μm × 649 μm from the center of registered images, focusing on our area of interest. The dry image was segmented into pore and grain. The segmented porosity (pore volume/total volume) was lower than the measured porosity due to the resolution (4.51 μm) of the CT machine. However, our analysis focused on macro-pores instead of micro-pores, which were beneficial for subsequent contact angle calculation (Selem et al., 2023). To establish adequate contrast between rock and fluid, wet images were subtracted by the pore space of the dry image, and we obtained an oil and brine map without rock, as shown in Fig. 4(b). This map was then segmented into two phases using a watershed segmentation algorithm (refer to Fig. 4(c)). Finally, oil, water, and rock were integrated into a slice (refer to Fig. 4(d)) to characterize contact angles, pore-scale fluid distribution, and oil clusters. The same procedure was applied to both HSW and LSW. It is worth mentioning that traditional methods were used for image processing in this study whereas deep learning will be tried in future works (Alqahtani et al., 2022; Soltanmohammadi and Faroughi, 2023).

2.4. Euler number and shape factor calculation

The Euler number (E) and shape factor (G) are indicative of the topology and geometry features of the remaining oil, respectively.

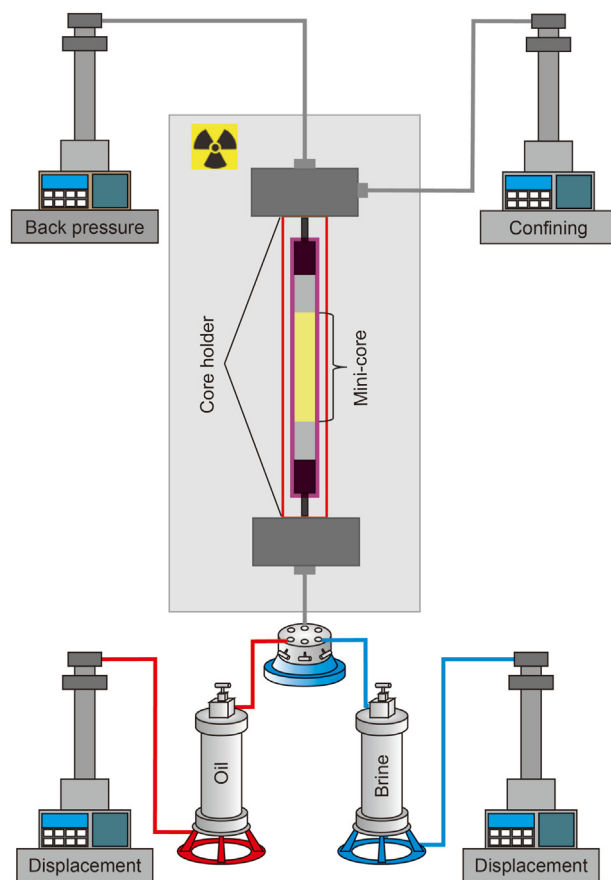


Fig. 2. Schematic of the experimental apparatus used for miniature core-flooding and scanning.

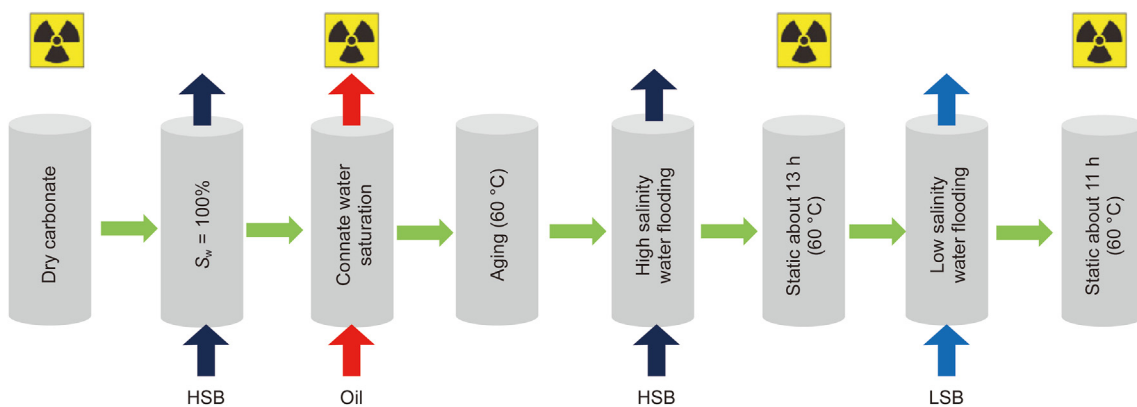


Fig. 3. An outline of experimental procedures.

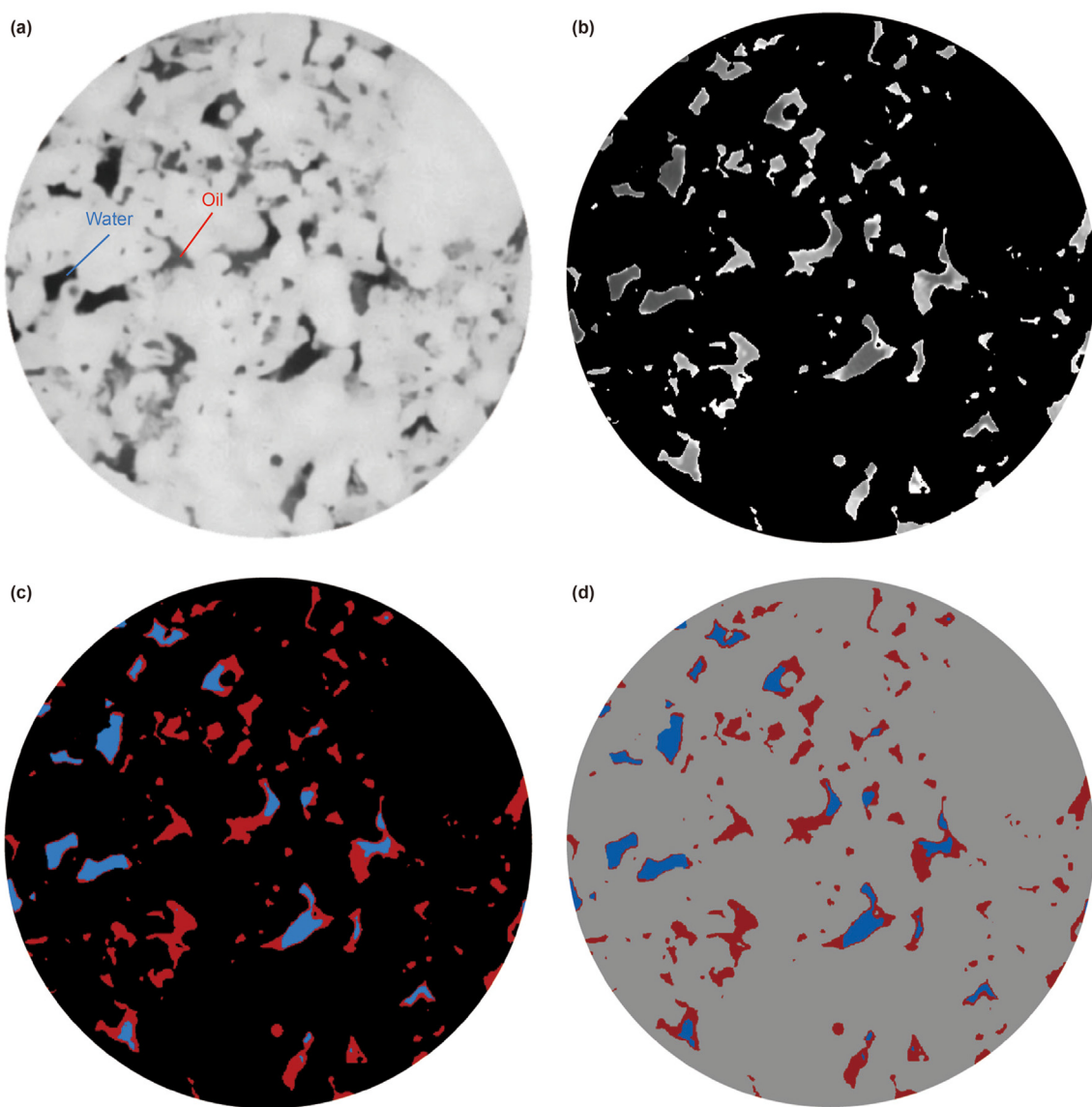


Fig. 4. Image processing workflow. (a) Original image at a resolution of 4.51 μm; (b) Fluid distribution without grain; (c) Segmented fluid distribution without grain where red and blue are oil and brine, respectively; (d) Integrated fluid and grain distribution where red, blue, and grey are oil, brine, and grain.

The shape factor, a dimensionless quantity, describes the degree to which the oil shape is similar to spheres. For instance, $G = 1$ when oil is spherical (Li et al., 2017). It can be obtained by defining the following formula in the label analysis module of Avizo (Guo et al., 2018; Yang et al., 2020):

$$G = \frac{6\sqrt{\pi}V}{A^{1.5}} \tag{1}$$

where G is the shape factor; V is the volume of oil, μm^3 ; A symbolizes the surface area of oil, μm^2 .

The Euler number is generally used to characterize the connectivity of the remaining oil and can be calculated using the label analysis module of Avizo. The smaller the Euler number, the better the connectivity of the oil.

$$E = \beta_0 - \beta_1 + \beta_2 \tag{2}$$

where β_0 represents the number of isolated components; β_1 represents the number of channels; β_2 represents the number of closed cavities (Yang et al., 2019; Qin et al., 2022).

The remaining oil was classified into four categories: network, multiple, singlet, and film (as shown in Table 3), based on shape factor and Euler number (Yang et al., 2020).

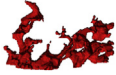



3. Results and discussion

3.1. Pore-scale displacement mechanism and fluid distribution

To evaluate the impact of LSW on wettability, contact angles were calculated using the algorithm implemented in OpenFOAM. This algorithm utilizes the geographic distribution of contact angles on fluid (oil and water) and rock contact lines from three-dimensional segmentation images to evaluate rock wettability (AlRatrouf et al., 2017, 2018a, 2018b). Fig. 5 exhibited the contact angle distribution after HSW and LSW. The number of angles between 0° and 40° was 21 at the end of HSW, whereas a total of 455 angles fell within this interval after LSW. We can also observe that the contact angle followed a normal distribution. Furthermore, the curve shifted to the left after LSW, indicating a wettability alteration. To confirm our findings, we calculated the average value, which was shifted from 127.47° to 108.22° during LSW, indicating that the rock was less oil-wet as well.

The variations in the interfacial area between the oil and rock also indicate the wettability characteristics of the rock. The interfacial area of the oil cluster consists of oil-rock and oil-brine interfacial areas, which were calculated using the following steps: The segmented oil image was dilated by one pixel, and the total interfacial area of the oil was obtained by subtracting the original oil image from the dilated oil image. Subsequently, the Boolean

Table 3
Classification of remaining oil: network, multiple, film, and singlet.

Type of remaining oil	Image	Classification standard
Network		$G \leq 0.3$
Multiple		$0.3 < G \leq 0.7$ & $E < 1$
Film		$0.3 < G \leq 0.7$ & $E \geq 1$
Singlet		$G > 0.7$

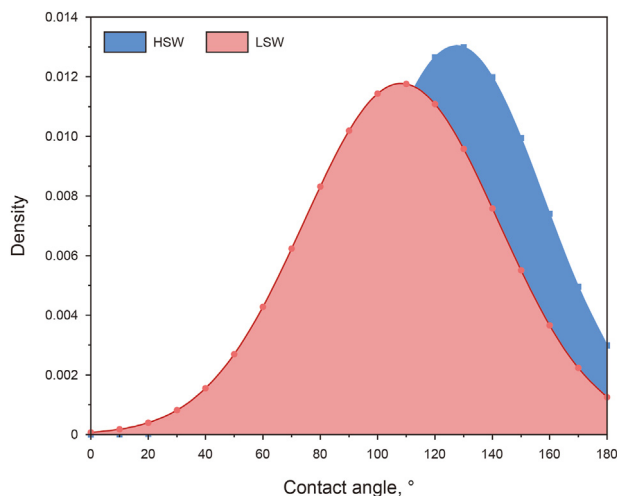


Fig. 5. Contact angle distribution calculated based on 3D images with a resolution of $4.51 \mu\text{m}$.

“AND” operation was applied to the dilated oil image and the segmented brine image to obtain the oil-brine interfacial area. The oil-rock interfacial area was calculated by subtracting the oil-brine interfacial area from the total oil interfacial area. Importantly, all operations were performed in Avizo. Table 4 presents the variations in oil interfacial area coverage at different displacement stages, normalized by the interfacial area of the oil. The fraction of interfacial area coverage between oil and rock changed from 0.879 to 0.789 after HSW and LSW, which was consistent with the distribution of contact angles. After both HSW and LSW, the oil exhibited a preference for contacting the rock due to its oil-wet nature, leading to a larger interfacial area.

The fluid configuration was further analyzed by comparing the pore-scale fluid occupancy maps at the end of HSW and LSW, as depicted in Fig. 6. The process of brine displacing oil in an oil-wet system is a piston-like displacement event. Capillary pressure (P_c), which is determined by the interfacial tension between oil and brine, pore geometry, and contact angles, acts as the resistance force (Qin et al., 2019). Some dead-end pores were bypassed even after LSW and remained filled with oil (see Fig. 6, type 1) because the threshold brine pressure needed to invade these pores was high. However, even though some pores were not invaded after HSW, they were invaded by LSB, resulting in a fluid configuration in which brine occupied the center of the pores and oil was trapped in the corners (Fig. 6, after LSW type 2). For type 2, a part of pore spaces was still occupied by oil after LSW, indicating oil-wet characterization. Additionally, the oil had been displaced from the center of the pores, forming a connected pathway for brine. Several parameters, such as pore geometry, interfacial tension, and injection rate, remained relatively unchanged. Therefore, wettability was the primary factor contributing to the different fluid configurations before and after LSW. Compared to type 1, type 2 (Fig. 6) suggested pore structure had a significant impact on the oil recovery improvement during LSW. Not only does brine displace oil, but oil also displaces water. The oil-filling event is also considered a

Table 4
Changes in oil surface area contacting rock and brine after HSW and LSW.

Oil interfacial area coverage (fraction)	HSW	LSW
Oil-rock	0.879	0.789
Oil-brine	0.121	0.210

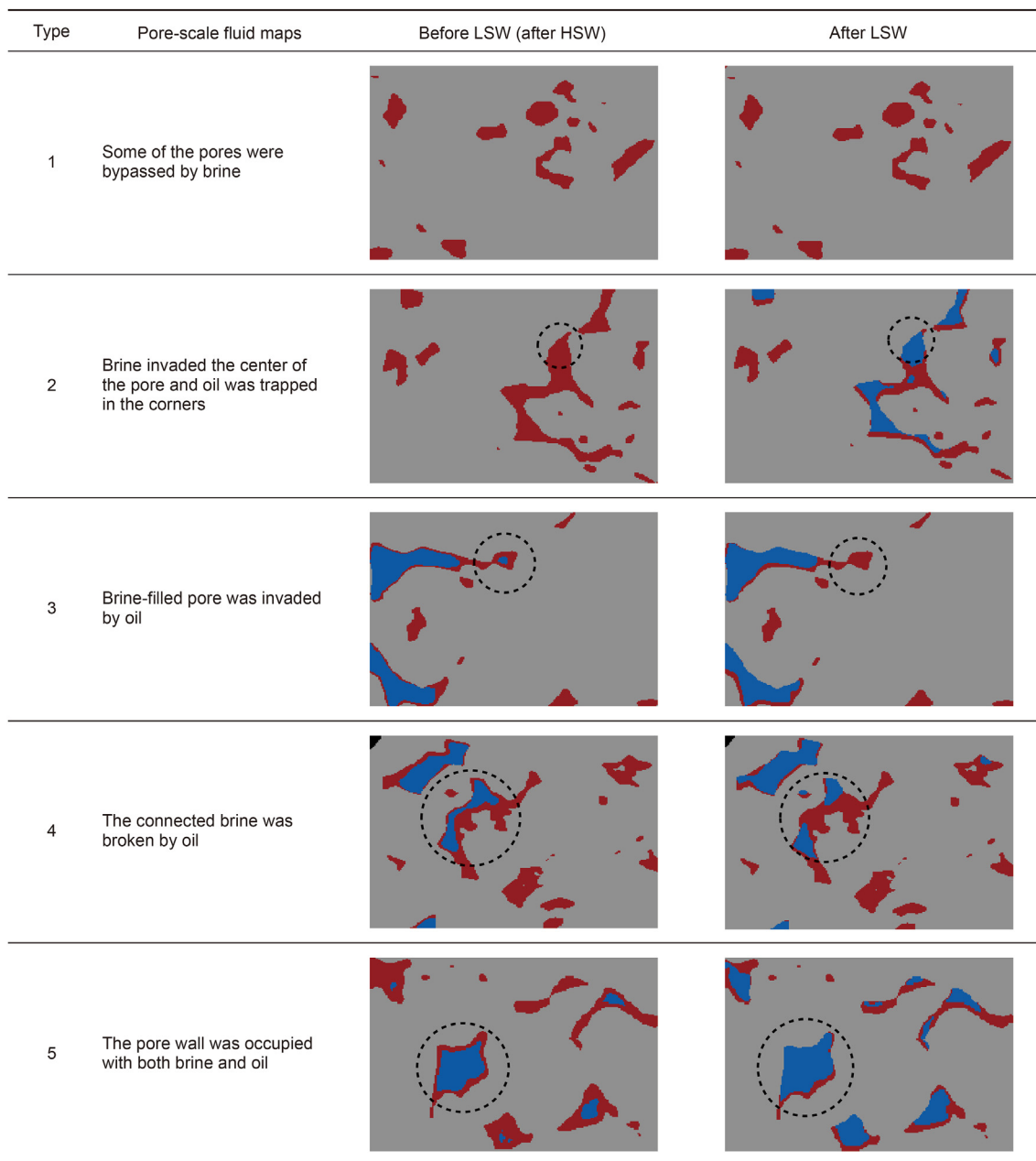


Fig. 6. Changes in the pore-scale fluid map before and after LSW (brine, oil, and rock are blue, red, and grey, respectively).

pore-scale displacement event, as illustrated in Fig. 6 (type 3). Meanwhile, we observed that the interconnected brine was displaced by oil, as depicted in Fig. 6 (type 4). The mobilized oil was re-trapped in Fig. 6 (types 3 and 4), which is probably due to the presence of snap-off events that are the signals of a more water-wet system (Andrews et al., 2021). In addition, the pore walls that were completely occupied by oil were transformed into oil-brine co-occupancies, as shown in Fig. 6 (type 5). The variation in oil film thickness aligned with the findings of Mohammadi and Mahani (2020), suggesting wettability alteration.

Furthermore, we utilized the advanced image analysis method proposed by Shabaninejad et al. (2018) to quantify the changes in the fluid map. For example, “OO” was calculated by intersecting sets of oil images after HSW and LSW. Then, the label analysis command

was used to determine the volume of “OO”. Here, “OO” represents pore spaces that were filled with oil after HSW and still were occupied by oil after LSW. On the other hand, “BB” represents pore spaces always filled with brine before and after LSW. Similarly, “BO” denotes the oil-filling process in which oil displaces brine. On the other hand, “OB” indicates the brine-filling event in which brine displaces oil, causing the pore spaces to be filled with brine after LSW. We found that the OO event accounted for 60% of the pore volume due to the oil-wet nature of the rock sample, while the BB event accounted for 18% of the pore volume, as shown in Fig. 7. There were only a few oil-filling events—just 2%. Comparatively, brine-filling events occurred more frequently.

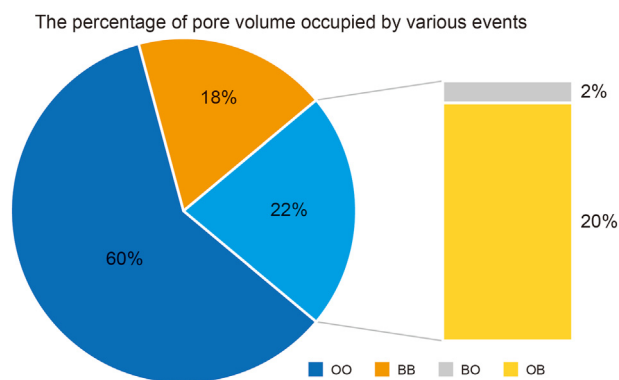


Fig. 7. Statistical analysis of fluid distribution after LSW. There were fewest oil-filling events (BO) and oil still occupied most pore volume (OO + BO).

3.2. Saturation and statistical analysis of remaining oil

3.2.1. Remaining oil saturation

Pore-scale displacement events affect the oil saturation and the size distribution of the remaining oil cluster. To assess the effectiveness of LSW, oil saturation (calculated as oil volume/pore volume) was determined using the volume fraction command in Avizo. Initially, the carbonate sample was almost completely saturated with oil, so the initial oil saturation was considered 100%. After HSW, the remaining oil saturation was 80%, while there was 61.6% remaining oil saturation at the end of LSW. In other words, the recovery improved by approximately 18.4%, which is in agreement with findings from previous studies. For example, Yousef et al. (2011) observed an 18% additional recovery in carbonate during tertiary LSW with 213,000 ppm formation water; Gupta et al. (2011) conducted tertiary LSW in carbonate and obtained a 20% recovery enhancement when formation water had a salinity of 181,273 ppm; Chandrasekhar et al. (2016) saturated limestone using formation water with 179,700 ppm and carried out LSW in the tertiary mode, reporting a 32% oil recovery factor. Furthermore, to investigate the impact of low-salinity brine on different positions of the carbonate sample, we plotted oil saturation curves that were obtained by stacking the saturation values, as shown in Fig. 8. It was observed that the oil saturation distribution at the end of HSW was

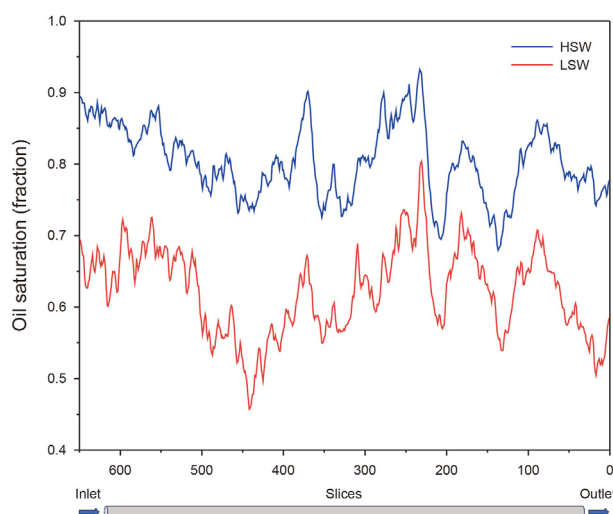


Fig. 8. Oil saturation distribution along the flow direction of brine at the end of HSW and LSW.

similar to that of LSW, exhibiting a significant resemblance to the porosity profile in Fig. 1(a). This suggested the interface between low-salinity brine and oil advanced uniformly, leading to the displacement of oil from the pores (Khishvand et al., 2017). Furthermore, there were several fluctuations in the oil saturation profile, which were strongly related to the flow field and porosity distribution (Mohamed et al., 2020).

3.2.2. Statistical analysis of the remaining oil cluster

Afterward, a statistical analysis of the remaining oil was conducted to gain a deep understanding of mass transfer and remobilization effects (Li et al., 2023). Larger oil clusters, which are easier to split into smaller ones, are easily remobilized. However, due to the smaller ratio of surface area-volume, larger oil clusters slow down the mass transfer (Jha et al., 2020). The label analysis module in Avizo was utilized to count the sizes and quantities of oil based on segmented images. Fig. 9(a) depicts the normalized frequency (calculated as $N/\text{total number of oil clusters}$) of remaining oil volume V . The distribution of oil cluster volume followed a power-law relationship, $N - V^{-\tau}$ (Iglauer et al., 2019). The power exponents (τ) for oil cluster distribution after HSW and LSW were 1.03 and 1.209, respectively. Iglauer et al. (2016) reported exponents (τ) ranging between 0.7 and 1.7 when measuring the oil-cluster-volume distribution. These exponents were much lower than the value predicted by the percolation theory value (i.e., $\tau = 2.189$). The τ after LSW was higher than after HSW (from 1.03 to 1.21), indicating that larger oil clusters broke into various smaller ones (Iglauer et al., 2019), in agreement with the pore fluid map (Fig. 6, type 2). We found that the number of small oil clusters in both HSW and LSW was significantly greater than in large oil clusters, especially after LSW. The increase in small oil clusters also led to the frequency of large oil clusters declining after LSW. Furthermore, the volume of the largest oil cluster after HSW was $1.11 \times 10^9 \mu\text{m}^3$ while it was $8.24 \times 10^8 \mu\text{m}^3$ after LSW. The volume did not change considerably.

We further calculated the surface and volume of the oil clusters and plotted the surface-volume distribution as shown in Fig. 9(b), which indicated an excellent fit of the power-law relationship ($R^2 > 0.98$)— $A-V^p$, in which after HSW and LSW, the values of p were 0.785 and 0.801, respectively. Furthermore, the surface area to volume ratio of the oil cluster was larger after LSW, indicating enhanced mass transfer between the oil and brine surface.

3.2.3. Pore occupancy

To probe the remaining oil distribution in various pore sizes, we quantified pore fluid occupancy. Firstly, the pores were categorized into three groups based on their equivalent diameter: less than 200 μm , between 200 and 400 μm , and greater than 400 μm . Importantly, these three groups had similar total pore volumes. In a pore of a specific size, the number of oil voxels was counted and divided by the total number of pore voxels. This allowed us to calculate the oil occupancy. By subtracting the oil occupancy from 1, we obtained the brine occupancy. According to this operation, we calculated all the pore fluid occupancy, as shown in Fig. 10. We found that more oil was trapped due to the reduction in pore diameter, whether it was after HSW or LSW. A low-salinity effect was observed in pores of different sizes. This effect was most pronounced in medium-sized pores (with an equivalent diameter between 200 and 400 μm), where 24.19% of the oil was displaced. Enhanced oil recovery during LSW is influenced by pore size distribution. A larger number of medium-sized pores result in better LSW performance (Qin et al., 2019). Also, the proportion of oil in small pores was more than in medium-sized pores and large pores even after LSW. This was attributed to the oil-wet nature of rock which caused the higher capillary pressure required for brine to invade these small pores.

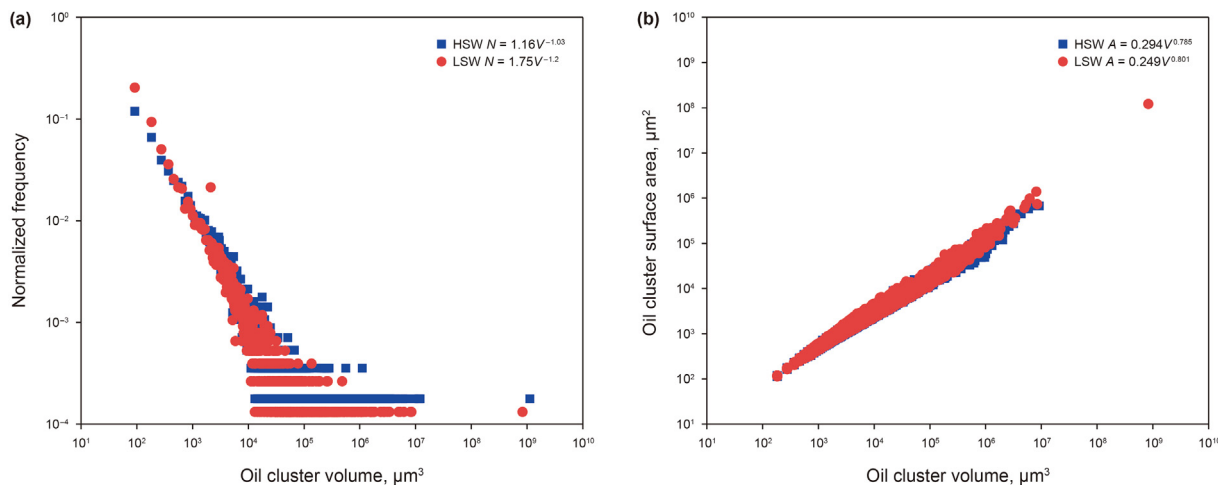


Fig. 9. Remaining oil cluster statistics after HSW and LSW. (a) Oil cluster volume distribution; (b) Oil cluster surface area-volume distribution.

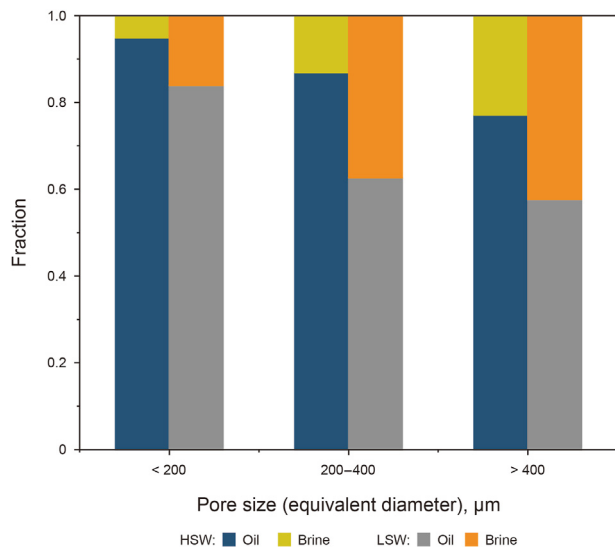


Fig. 10. Pore occupancy of oil and brine in different pore sizes.

3.3. Classification of remaining oil clusters

Fig. 11 provides a visualization and a related calculation of the remaining oil. After LSW, the remaining oil volume decreased by $0.33 \times 10^9 \mu\text{m}^3$. The Euler number became more negative, indicating that the connectivity of the oil phase became better, which was consistent with findings by Qin et al. (2021) and was beneficial for subsequent recovery. The number of networks, films, and singlets increased with LSW while decreasing in volume, which was consistent with changes in the volume fraction. Multiple counts, volume, and volume fraction varied oppositely from the other three types of remaining oil. As shown in Fig. 12, the network was dominant and accounted for 88.5% and 88.47% of the total remaining oil volume after HSW and LSW, respectively. Networks with well-connected shapes spanning multiple pores are the easiest forms to be mobilized (She et al., 2021). Although the volume fraction of the network remained fairly constant, this trend is comparable with previous studies, which proved networks were the primary contributor to the total remaining oil (Su et al., 2022). The volume fraction of film and singlet decreased after LSW, which

was different from conventional waterflooding. The film adhered to the rock surface continuously in the form of a film, but detached as a result of wettability alteration. Meanwhile, singlet, located in dead-end regions, was mobilized because the oil moved to larger pores due to mixing between HSB and LSB (Aziz et al., 2020). Film and singlet remaining oil are extremely difficult to mobilize. However, there were relatively large volume fraction variations, which reflect the characteristics of enhanced oil recovery of LSB. There was an increase in the multiple volume fraction, which may be caused by the coalescence of singlet (Aziz et al., 2020) or film.

4. Conclusions

In this study, micro-CT was utilized to acquire images of various displacement stages during tertiary low-salinity waterflooding in a carbonate. The main conclusions have been drawn.

- (1) The contact angles between oil, brine, and rock shift from 127.47° to 108.22° during low-salinity waterflooding, representing a substantial change of 19.25° . After low-salinity waterflooding, the oil-rock surface area decreased by 9%. From the fluid configuration, we observed that the pore wall, previously occupied by oil, was now being occupied by both brine and oil.
- (2) The relationships between normalized frequency (N /total number of oil clusters) and remaining oil volume (V) were well-fitted ($R^2 > 0.98$) by a power-law correlation. After high-salinity waterflooding and low-salinity waterflooding, the power exponents were 0.785 and 0.801, respectively. The surface-volume distribution of the oil cluster indicated a higher surface area-to-volume ratio after low-salinity waterflooding, which increased mass transfer between the oil and brine surfaces.
- (3) Low-salinity brine can displace oil from small, medium, and large pores. This effect was most pronounced in medium-sized pores, where 24.19% of the oil was displaced. Therefore, a greater number of medium-sized pores contributes to better low-salinity waterflooding performance.
- (4) We classified the remaining oil into network, multiple, singlet, and film. There were reductions in film and singlet remaining oil. Furthermore, the connectivity of the remaining oil after low-salinity waterflooding improved, which was beneficial for further recovery improvement.

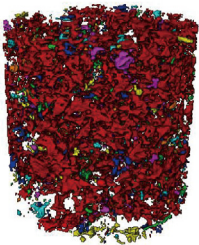
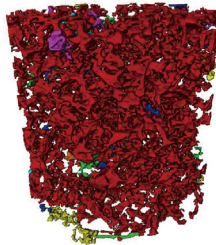

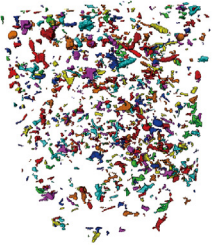

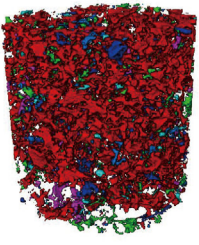
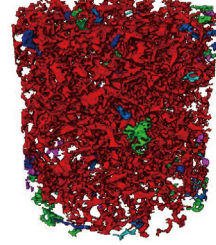
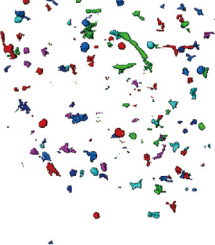
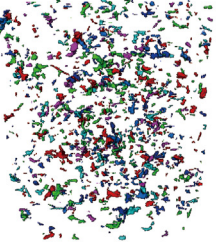
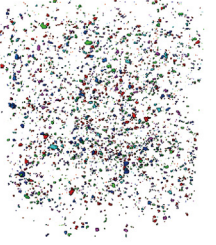
	Remaining oil	Network	Multiple	Film	Singlet
HSW	 $E = -3815$ Volume = $1.42 \times 10^9 \mu\text{m}^3$	 Count = 86 Volume = $1.25 \times 10^9 \mu\text{m}^3$	 Count = 69 Volume = $2.12 \times 10^7 \mu\text{m}^3$	 Count = 1023 Volume = $1.09 \times 10^8 \mu\text{m}^3$	 Count = 4449 Volume = $3.22 \times 10^7 \mu\text{m}^3$
LSW	 $E = -6882$ Volume = $1.09 \times 10^9 \mu\text{m}^3$	 Count = 144 Volume = $9.65 \times 10^8 \mu\text{m}^3$	 Count = 28 Volume = $2.89 \times 10^7 \mu\text{m}^3$	 Count = 1056 Volume = $7.53 \times 10^7 \mu\text{m}^3$	 Count = 6143 Volume = $2.16 \times 10^7 \mu\text{m}^3$

Fig. 11. 3D images and related calculations of remaining oil. Each color represents a disconnected oil cluster.

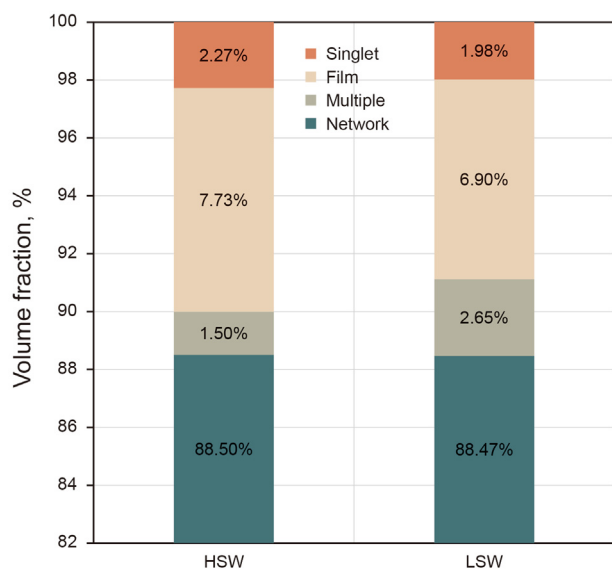


Fig. 12. Volume fraction of different types of remaining oil.

CRedit authorship contribution statement

Chun-Yu Tong: Writing – review & editing, Writing – original draft, Visualization, Software, Methodology, Data curation. **Yong-Fei Yang:** Supervision, Resources, Project administration, Conceptualization. **Qi Zhang:** Writing – review & editing, Software, Methodology, Data curation. **Gloire Imani:** Validation. **Lei Zhang:** Validation, Data curation. **Hai Sun:** Supervision, Formal analysis. **Jun-Jie Zhong:** Supervision, Formal analysis. **Kai Zhang:** Supervision. **Jun Yao:** Supervision, Formal analysis.

Declaration of competing interest

We declare that we have no financial and personal relationships with other people or organizations that can inappropriately influence our work, there is no professional or other personal interest of any nature or kind in any product, service and/or company that could be construed as influencing the position presented in, or the review of, the manuscript entitled.

Acknowledgments

We would like to express appreciation to the following financial support: the National Key Research and Development Program of China (2022YFE0203400), the National Natural Science Foundation of China (Nos. U23A20595, 52034010, 52288101), the Qingdao Natural Science Foundation (No. 23-2-1-230-zyyd-jch), the Fundamental Research Funds for the Central Universities (No. 23CX10004A), and the Program for Changjiang Scholars and Innovative Research Team in University (No. IRT_16R69).

References

Akbar, M., Vissapragada, B., Alghamdi, A.H., et al., 2000. A snapshot of carbonate reservoir evaluation. *Oilfield Rev.* 12, 20–41.
 Alqahtani, N.J., Niu, Y., Wang, Y.D., et al., 2022. Super-resolved segmentation of X-ray images of carbonate rocks using deep learning. *Transport Porous Media* 143 (2), 497–525. <https://doi.org/10.1007/s11242-022-01781-9>.
 AlRatrou, A., Raeini, A.Q., Bijeljic, B., et al., 2017. Automatic measurement of contact angle in pore-space images. *Adv. Water Resour.* 109, 158–169. <https://www.sciencedirect.com/science/article/pii/S0309170817303342>.
 AlRatrou, A., Blunt, M.J., Bijeljic, B., 2018a. Spatial correlation of contact angle and curvature in pore-space images. *Water Resour. Res.* 54 (9), 6133–6152. <https://agupubs.onlinelibrary.wiley.com/doi/abs/10.1029/2017WR022124>.
 AlRatrou, A., Blunt, M.J., Bijeljic, B., 2018b. Wettability in complex porous materials, the mixed-wet state, and its relationship to surface roughness. *Proc. Natl. Acad. Sci. USA* 115 (36), 8901–8906. <https://www.pnas.org/doi/abs/10.1073/pnas.1803734115>.
 Andrews, E., Muggerridge, A., Garfi, G., et al., 2021. Pore-scale X-ray imaging of wetting alteration and oil redistribution during low-salinity flooding of Berea

- sandstone. *Energy Fuels* 35 (2), 1197–1207. <https://doi.org/10.1021/acs.energyfuels.0c03299>.
- Andrews, E., Muggerridge, A., Jones, A., et al., 2023. Pore structure and wetting alteration combine to produce the low salinity effect on oil production. *Fuel* 332, 126155. <https://www.sciencedirect.com/science/article/pii/S0016236122029799>.
- Ayrala, S.C., Yousef, A.A., Li, Z., et al., 2018a. Coalescence of crude oil droplets in brine systems: effect of individual electrolytes. *Energy Fuels* 32 (5), 5763–5771. <https://doi.org/10.1021/acs.energyfuels.8b00309>.
- Ayrala, S.C., Al-Saleh, S.H., Al-Yousef, A.A., 2018b. Microscopic scale interactions of water ions at crude oil/water interface and their impact on oil mobilization in advanced water flooding. *J. Petrol. Sci. Eng.* 163, 640–649. <https://www.sciencedirect.com/science/article/pii/S0920410517307519>.
- Aziz, R., Niasar, V., Erfani, H., et al., 2020. Impact of pore morphology on two-phase flow dynamics under wettability alteration. *Fuel* 268, 117315. <https://www.sciencedirect.com/science/article/pii/S0016236120303100>.
- Bartels, W.-B., Mahani, H., Berg, S., et al., 2017a. Oil configuration under high-salinity and low-salinity conditions at pore scale: a parametric investigation by use of a single-channel micromodel. *SPE J.* 22 (5), 1362–1373. <https://doi.org/10.2118/181386-PA>.
- Bartels, W.-B., Rücker, M., Berg, S., et al., 2017b. Fast X-ray micro-CT study of the impact of brine salinity on the pore-scale fluid distribution during waterflooding. *Petrophysics* 58 (1), 36–47.
- Bartels, W.-B., Ruecker, M., Berg, S., et al., 2016. Micro-CT study of the impact of low salinity waterflooding on the pore-scale fluid distribution during flow. *International Symposium of the Society of Core Analysts held in Snowmass 21–26. Colorado, USA, August 2016*.
- Berg, S., Cense, A.W., Jansen, E., et al., 2010. Direct experimental evidence of wettability modification by low salinity. *Petrophysics* 51 (5).
- Blunt, M.J., 2017. *Multiphase Flow in Permeable Media: A Pore-Scale Perspective*. Cambridge University Press, Cambridge. <https://doi.org/10.1017/9781316145098>.
- Chandrasekhar, S., Sharma, H., Mohanty, K.K., 2016. Wettability alteration with brine composition in high temperature carbonate rocks. *SPE Annual Technical Conference and Exhibition*. <https://doi.org/10.2118/181700-MS>.
- Chen, Y., Jha, N.K., Lebedev, M., et al., 2021. Integral effects of initial fluids configuration and wettability alteration on remaining saturation: characterization with X-ray micro-computed tomography. *Fuel* 306, 121717. <https://www.sciencedirect.com/science/article/pii/S0016236121015982>.
- Dong, H., Blunt, M.J., 2009. Pore-network extraction from micro-computerized-tomography images. *Phys. Rev.* 80 (3), 036307. <https://link.aps.org/doi/10.1103/PhysRevE.80.036307>.
- Farhadi, H., Ayatollahi, S., Fatemi, M., 2021. The effect of brine salinity and oil components on dynamic IFT behavior of oil-brine during low salinity water flooding: diffusion coefficient, EDL establishment time, and IFT reduction rate. *J. Petrol. Sci. Eng.* 196, 107862. <https://www.sciencedirect.com/science/article/pii/S0920410520309220>.
- Guo, C., Wang, X., Wang, H., et al., 2018. Effect of pore structure on displacement efficiency and oil-cluster morphology by using micro computed tomography (μ CT) technique. *Fuel* 230, 430–439. <https://www.sciencedirect.com/science/article/pii/S0016236118308810>.
- Gupta, R., Smith, P.G., Hu, L., et al., 2011. Enhanced waterflood for Middle East carbonate cores — impact of injection water composition. *SPE Middle East Oil and Gas Show and Conference*. <https://doi.org/10.2118/142668-MS>.
- Haagh, M.E.J., Siretanu, I., Duits, M.H.G., et al., 2017. Salinity-Dependent contact angle alteration in oil/brine/silicate systems: the critical role of divalent cations. *Langmuir* 33 (14), 3349–3357. <https://doi.org/10.1021/acs.langmuir.6b04470>.
- Hiorth, A., Cathles, L.M., Madland, M.V., 2010. The impact of pore water chemistry on carbonate surface charge and oil wettability. *Transport Porous Media* 85 (1), 1–21. <https://doi.org/10.1007/s11242-010-9543-6>.
- Iglauer, S., Rahman, T., Sarmadivaleh, M., et al., 2016. Influence of wettability on residual gas trapping and enhanced oil recovery in three-phase flow: a pore-scale analysis by use of microcomputed tomography. *SPE J.* 21 (6), 1916–1929. <https://doi.org/10.2118/179727-PA>.
- Iglauer, S., Paluszny, A., Rahman, T., et al., 2019. Residual trapping of CO₂ in an oil-filled, oil-wet sandstone core: results of three-phase pore-scale imaging. *Geophys. Res. Lett.* 46 (20), 11146–11154. <https://agupubs.onlinelibrary.wiley.com/doi/abs/10.1029/2019GL083401>.
- Jha, N.K., Lebedev, M., Iglauer, S., et al., 2020. Pore scale investigation of low salinity surfactant nanofluid injection into oil saturated sandstone via X-ray micro-tomography. *J. Colloid Interface Sci.* 562, 370–380. <https://www.sciencedirect.com/science/article/pii/S0021979719315000>.
- Kargarpour, M., 2020. Carbonate reservoir characterization: an integrated approach. *J. Pet. Explor. Prod. Technol.* 10, 2655–2667. <https://doi.org/10.1007/s13202-020-00946-w>.
- Khishvand, M., Alizadeh, A.H., Oraki Kohshour, I., et al., 2017. In situ characterization of wettability alteration and displacement mechanisms governing recovery enhancement due to low-salinity waterflooding. *Water Resour. Res.* 53 (5), 4427–4443. <https://agupubs.onlinelibrary.wiley.com/doi/abs/10.1002/2016WR020191>.
- Koleini, M.M., Badizad, M.H., Kargozarfard, Z., et al., 2019. Interactions between rock/brine and oil/brine interfaces within thin brine film wetting carbonates: a molecular dynamics simulation study. *Energy Fuels* 33 (9), 7983–7992. <https://doi.org/10.1021/acs.energyfuels.9b00496>.
- Lager, A., Webb, K.J., Black, C.J., et al., 2008. Low salinity oil recovery - an experimental investigation. *Petrophysics* 49 (1), 28–35.
- Lebedeva, E.V., Fogden, A., 2011. Micro-CT and wettability analysis of oil recovery from sand packs and the effect of waterflood salinity and kaolinite. *Energy Fuels* 25 (12), 5683–5694. <https://doi.org/10.1021/ef201242s>.
- Li, J., Jiang, H., Wang, C., et al., 2017. Pore-scale investigation of microscopic remaining oil variation characteristics in water-wet sandstone using CT scanning. *J. Nat. Gas Sci. Eng.* 48, 36–45. <https://www.sciencedirect.com/science/article/pii/S1875510017301725>.
- Li, Y., Yang, Y., Dong, M., et al., 2023. In-situ imaging of CO₂ trapping and oil recovery in three-phase systems: dependence on pore geometry and wettability. *SPE J.* 28 (2), 768–782. <https://doi.org/10.2118/212830-PA>.
- Lyu, C., Zhong, L., Ning, Z., et al., 2022. Review on underlying mechanisms of low salinity waterflooding: comparisons between sandstone and carbonate. *Energy Fuels* 36 (5), 2407–2423. <https://doi.org/10.1021/acs.energyfuels.1c04248>.
- Mahzari, P., Sohrabi, M., 2014. Crude oil/brine interactions and spontaneous formation of micro-dispersions in low salinity water injection. *SPE Improved Oil Recovery Symposium*. <https://doi.org/10.2118/169081-MS>.
- Mehana, M., Fahes, M., Kang, Q., et al., 2020. Molecular simulation of double layer expansion mechanism during low-salinity waterflooding. *J. Mol. Liq.* 318, 114079. <https://www.sciencedirect.com/science/article/pii/S0167732220314896>.
- Mirchi, V., 2018. Pore-scale investigation of the effect of surfactant on fluid occupancies during low-salinity waterflooding in oil-wet carbonates. *SPE Annual Technical Conference and Exhibition*. <https://doi.org/10.2118/194045-STU>.
- Mohamed, A.I.A., Khishvand, M., Piri, M., 2020. A pore-scale experimental investigation of process-dependent capillary desaturation. *Adv. Water Resour.* 144, 103702. <https://www.sciencedirect.com/science/article/pii/S0309170820300609>.
- Mohammadi, M., Mahani, H., 2020. Direct insights into the pore-scale mechanism of low-salinity waterflooding in carbonates using a novel calcite microfluidic chip. *Fuel* 260, 116374. <https://www.sciencedirect.com/science/article/pii/S0016236119317284>.
- Mokhtari, R., Ayatollahi, S., Fatemi, M., 2019. Experimental investigation of the influence of fluid-fluid interactions on oil recovery during low salinity water flooding. *J. Petrol. Sci. Eng.* 182, 106194. <https://www.sciencedirect.com/science/article/pii/S0920410519306060>.
- Nasralla, R.A., Nasr-El-Din, H.A., 2014. Double-layer expansion: is it a primary mechanism of improved oil recovery by low-salinity waterflooding? *SPE Reservoir Eval. Eng.* 17 (1), 49–59. <https://doi.org/10.2118/154334-PA>.
- Qin, T., Fenter, P., Alotaibi, M., et al., 2021. Pore-scale oil connectivity and displacement by controlled-ionic-composition waterflooding using synchrotron X-ray microtomography. *SPE J.* 26 (6), 3694–3701. <https://doi.org/10.2118/201618-PA>.
- Qin, X., Xia, Y., Wu, J., et al., 2022. Influence of pore morphology on permeability through digital rock modeling: new insights from the Euler number and shape factor. *Energy Fuels* 36 (14), 7519–7530. <https://doi.org/10.1021/acs.energyfuels.2c01359>.
- Qin, Z., Arshadi, M., Piri, M., 2019. Micro-scale experimental investigations of multiphase flow in oil-wet carbonates. I. In situ wettability and low-salinity waterflooding. *Fuel* 257, 116014. <https://www.sciencedirect.com/science/article/pii/S0016236119313687>.
- Selem, A.M., Agenet, N., Gao, Y., et al., 2021. Pore-scale imaging and analysis of low salinity waterflooding in a heterogeneous carbonate rock at reservoir conditions. *Sci. Rep.* 11 (1), 15063. <https://doi.org/10.1038/s41598-021-94103-w>.
- Selem, A.M., Agenet, N., Blunt, M.J., et al., 2022. Pore-scale processes in tertiary low salinity waterflooding in a carbonate rock: micro-dispersions, water film growth, and wettability change. *J. Colloid Interface Sci.* 628, 486–498. <https://www.sciencedirect.com/science/article/pii/S0021979722010426>.
- Selem, A.M., Agenet, N., Foroughi, S., et al., 2023. Pore-scale imaging of emulsification of oil during tertiary and secondary low salinity waterflooding in a reservoir carbonate. *Energy Fuels* 37 (21), 16368–16377. <https://doi.org/10.1021/acs.energyfuels.3c02317>.
- Shabaninejad, M., Middlelton, J., Fogden, A., 2018. Systematic pore-scale study of low salinity recovery from Berea sandstone analyzed by micro-CT. *J. Petrol. Sci. Eng.* 163, 283–294. <https://www.sciencedirect.com/science/article/pii/S092041051731029X>.
- She, Y., Zhang, C., Mahardika, M.A., et al., 2021. Pore-scale study of in-situ surfactant flooding with strong oil emulsification in sandstone based on X-ray micro-tomography. *J. Ind. Eng. Chem.* 98, 247–261. <https://www.sciencedirect.com/science/article/pii/S1226086X21001696>.
- Smalley, P.C., Muggerridge, A.H., Dalland, M., et al., 2018. Screening for EOR and estimating potential incremental oil recovery on the Norwegian continental shelf. *SPE Improved Oil Recovery Conference*. <https://doi.org/10.2118/190230-MS>.
- Sohrabi, M., Mahzari, P., Farzaneh, S.A., et al., 2017. Novel insights into mechanisms of oil recovery by use of low-salinity-water injection. *SPE J.* 22 (2), 407–416. <https://doi.org/10.2118/172778-PA>.
- Soltanmohammadi, R., Faroughi, S.A., 2023. A comparative analysis of super-resolution techniques for enhancing micro-CT images of carbonate rocks. *Applied Computing and Geosciences* 20, 100143. <https://www.sciencedirect.com/science/article/pii/S2590197423000320>.
- Su, Y., Zha, M., Jiang, L., et al., 2022. Pore structure and fluid distribution of tight sandstone by the combined use of SEM, MICP and X-ray micro-CT. *J. Petrol. Sci. Eng.* 208, 109241. <https://www.sciencedirect.com/science/article/pii/S0920410521008949>.

- Tawfik, M.S., Karpyn, Z.T., Johns, R.T., 2022. Effect of oil chemistry on the performance of low-salinity waterflooding in carbonates: an integrated experimental approach. *Fuel* 329, 125436. <https://www.sciencedirect.com/science/article/pii/S0016236122022694>.
- Tetteh, J.T., Brady, P.V., Barati Ghahfarokhi, R., 2020. Review of low salinity waterflooding in carbonate rocks: mechanisms, investigation techniques, and future directions. *Adv. Colloid Interface Sci.* 284, 102253. <https://www.sciencedirect.com/science/article/pii/S000186862030275X>.
- Webb, K.J., Black, C.J.J., Al-Ajeel, H., 2004. Low salinity oil recovery – log-inject-log. SPE/DOE Symposium on Improved Oil Recovery. <https://doi.org/10.2118/89379-MS>.
- Wei, B., Wu, R., Lu, L., et al., 2017. Influence of individual ions on oil/brine/rock interfacial interactions and oil–water flow behaviors in porous media. *Energy Fuels* 31 (11), 12035–12045. <https://doi.org/10.1021/acs.energyfuels.7b02458>.
- Xu, Z.-X., Li, S.-Y., Li, B.-F., et al., 2020. A review of development methods and EOR technologies for carbonate reservoirs. *Petrol. Sci.* 17 (4), 990–1013. <https://doi.org/10.1007/s12182-020-00467-5>.
- Yang, Y., Yang, H., Tao, L., et al., 2019. Microscopic determination of remaining oil distribution in sandstones with different permeability scales using computed tomography scanning. *J. Energy Resour. Technol.* 141 (9), 092903. <https://doi.org/10.1115/1.4043131>.
- Yang, Y., Tao, L., Iglauer, S., et al., 2020. Quantitative statistical evaluation of micro residual oil after polymer flooding based on X-ray micro computed-tomography scanning. *Energy Fuels* 34 (9), 10762–10772. <https://doi.org/10.1021/acs.energyfuels.0c01801>.
- Yousef, A.A., Al-Saleh, S., Al-Kaabi, A., et al., 2011. Laboratory investigation of the impact of injection-water salinity and ionic content on oil recovery from carbonate reservoirs. *SPE Reservoir Eval. Eng.* 14 (5), 578–593. <https://doi.org/10.2118/137634-PA>.